Scripta Materialia 187 (2020) 323–328

Contents lists available at ScienceDirect

Scripta Materialia

journal homepage: www.elsevier.com/locate/scriptamat

Thickness-dependent shear localization in Cu/Nb metallic nanolayered composites

Shujing Dong[a], Tianju Chen[b], Sixie Huang[b], Nan Li[c], Caizhi Zhou[a,*]

[a] Department of Mechanical Engineering, University of South Carolina, Columbia, SC 29208, USA
[b] Department of Materials Science and Engineering, Missouri University of Science and Technology, Rolla, MO 65409, USA
[c] MPA-CINT, Los Alamos National Laboratory, Los Alamos, NM 87545, USA

ARTICLE INFO

Article history:
Received 5 April 2020
Revised 12 June 2020
Accepted 15 June 2020
Available online 28 June 2020

Keywords:
Metallic nanolayered composites
Molecular dynamics simulation
Shear localization
Size effect

ABSTRACT

We performed molecular dynamics simulations to study the effect of the layer thickness on the shear localization in Cu/Nb metallic nanolayered composites (MNCs). Our simulation results achieve good agreement with experimental results that the inverse size effect in the strength occurs in samples with layer thickness below 2.0 nm. The strain softening observed in those samples was triggered by the shear localization. The quantitative analysis revealed that the unsymmetrical dislocation transmission across the interface induces the shear localization and promotes the shear band formation in Cu/Nb MNCs. The plastic strain mainly comes from the interface sliding within the shear band.

Metallic nanolayered composites (MNCs) are a special class of composite materials made from alternative layers of different metallic constituents with the layer thickness at nanometer length scales [1–5]. As the interface can act as sinks and sources of defects during deformation, it plays a critical role in mechanical properties of MNCs, such as strength, fracture toughness and radiation damage resistance [6–10]. Mechanical testing results showed that MNCs exhibited 5–10 times higher strengths than their single phase counterparts and a clear size effect of increasing strength with decreasing the layer thickness, h [11–14]. However, several recent studies have shown clear length scale-dependent plastic deformation instability in MNCs, as the shear band formed in samples with h below a certain critical value [15–17]. In Cu/Ta MNCs, shear bands were observed in the samples with layer thicknesses below 10 nm under indentation and relevant to layer-buckling-induced GB sliding or rotation [16]. Recent rolling experiments illustrated that the shear bands appeared in Cu/Nb MNCs with $h = 4$ nm, while 40 nm samples can be uniformly deformed without the formation of shear bands [18]. Further micropillar compression test revealed that the strain within the shear band is four times higher than that away from the shear band [19]. The formation of local shear bands strongly affects the uniform deformability of MNCs that limits their applications [20–25]. Several scenarios have been proposed to explain the shear band formation in MNCs, such as dislocation transmission across the interface [20,22], sliding of columnar grains [24–26] and localized rotation of interfaces [21,23]. However, it is still unclear (i) how the layer thickness affects the shear localization in MNCs, (ii) what the role of the interface is during the shear band formation, and (iii) how the defects evolve within the shear band.

Molecular dynamics (MD) simulations offer a powerful tool to investigate the properties and microstructure evolution of materials at the nanoscale. In the case of MNCs, MD simulations have been used to identify the interface dislocation patterns [27–30], dislocation nucleation processes [31,32], interactions between dislocations and interfaces [33,34], and shear resistance of different types of interfaces [23,35,36]. Nevertheless, less attention has been paid to the formation of shear banding and the defect evolution in MNCs during deformation. In this work, we perform MD simulations to explore the effect of layer thicknesses on the shear localization in Cu/Nb MNCs during the pillar compression test.

Pillars consisted of Cu and Nb crystals were used in this study with h varying from 0.85 nm to 10 nm shown in Fig. 1(a)–(c). The {111} Kurdjumov-Sachs (KS) orientation relationship was adopted in our model as it is well-characterized in Cu/Nb MNCs fabricated by PVD [37]. The height and diameter of each pillar were set to be about 40 nm and 30 nm, respectively, as shown in Fig. 1. Periodic boundary condition was applied along the cylindrical axis, while the pillar surfaces were set to be stress free. Atomistic simulations were carried out by using LAMMPS with embedded atom method (EAM) potentials for Cu-Nb system developed in [38–40]. OVITO was used for the visualization of atomic structures [41]. The uniaxial compression deformation was carried out along the cylin-

* Corresponding author.
E-mail address: caizhi@mailbox.sc.edu (C. Zhou).

https://doi.org/10.1016/j.scriptamat.2020.06.049
1359-6462/

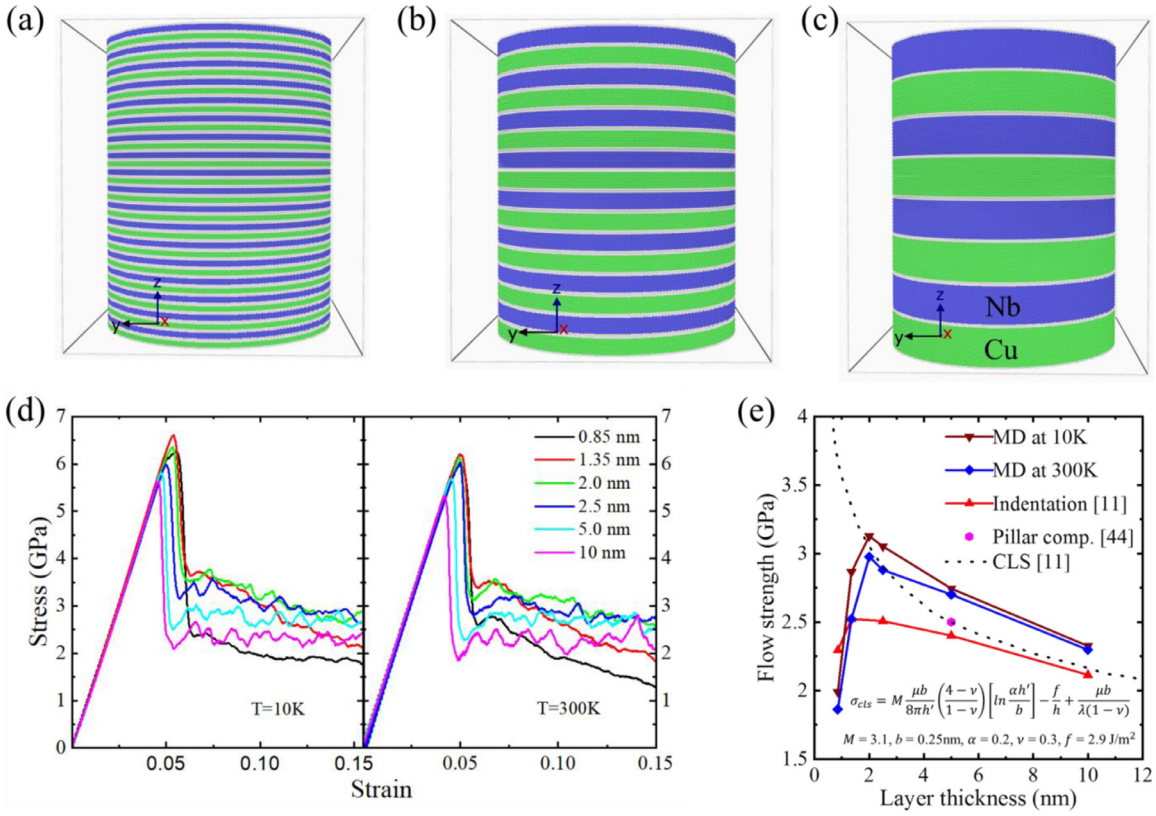

Fig. 1. The initial atomistic configurations of sample with (a) h = 0.85 nm, (b) h = 2.0 nm and (c) h = 5.0 nm. All samples have the crystallographic orientation of $[\bar{1}11]_{Nb}||[1\bar{1}0]_{Cu}$ along y-axis, $[1\bar{1}2]_{Nb}||[11\bar{2}]_{Cu}$ along x-axis and $[110]_{Nb}||[111]_{Cu}$ along z-axis. Atoms are colored by Common Neighbor Analysis (CNA). (d) Stress–strain curves for different samples at 10 K and 300 K. (e) Comparison of the MD averaged flow stress vs. layer thickness with the experimental data from ref. [11,44].

drical axis direction at a constant strain rate of 1.0×10^8 s^{-1} for two different temperatures (10 K and 300 K). Prior to deformation, all samples were relaxed for 400 ps under zero pressure with the isothermal-isobaric (NPT) ensemble. Before systematic study of the layer thickness effect, we performed calculations on pillars with different diameters, and the results confirmed that there is no pillar size effect on our simulation results (see Supplementary Material 1).

Fig. 1(d) shows stress-strain curves for all samples deformed at 10 K and 300 K. In all cases, before the elastic-plastic transition, the stress continues to rise with strain, reaches a peak value, and then drops after about 5% strain. The peak value appearing before plastic flow is typical in the MD simulations for nanostructures and relevant to the high strain rate imposed in the simulations [42]. Besides that, the defect-free samples used in our simulation may also induce the stress overshoot on the stress-strain curves, as experimental samples may contain a certain number of dislocations before deformation that can be easily activated under loading. Thus, we elect to use the flow stress averaged within the strain range of 7–15% as a measure of Cu/Nb MNCs strength in our simulations in Fig. 1(e). It is clear that, the size scaling in flow strength with h is not monotonic, with a positive effect of finer h leading to stronger material up to a critical layer thickness, h_c, below which the effect is reversed, and finer h leads to a weaker material (inverse size effect on the strength). Our simulation results show the same trend of the scaling and critical layer thickness, h_c ($\approx$ 2.0 nm) as those observed in experiments [11,43,44]. In addition, Fig. 1(d) illustrate that the stress achieves a plateau for $h > h_c$ during the plastic flow, while continues to drop with the strain (strain softening) for $h < h_c$. Based on an elasticity dislocation theory, Misra et al. proposed that for h < 100 nm, the plastic deformation in MNCs is generated by single dislocation threading within the layered phase (confined layer slip, CLS). While for $h < h_c$, the stress for CLS exceeds the stress for the dislocation transmission across the interface and the dislocation transmission mechanism controls the plastic deformation [11,12]. As shown in Fig. 1(e), the CLS model can match the general trend of experiment and simulation data at $h > h_c$, while it is not applicable at $h < h_c$. Our simulation results reveal that the strain softening for samples with $h < h_c$ is relevant to the dislocation transmission mechanism that induces the inverse size effect on the strength.

Fig. 2 compares the representative microstructures in the deformed samples with layer thicknesses below and above h_c, respectively. These microstructures were taken at the similar strain levels marked on the corresponding stress-strain curves in Fig. 2(a). It is clear that the onset of the plastic deformation marked as Fig. 2 (b-i) and (b-i') on the stress-strain curves was induced by the nucleation and propagation of dislocations from the free surface on both samples. For $h > h_c$, once the dislocations nucleated from the surface, they glided through the layered phase and deposited straight dislocation lines on the interface (see Supplementary movie 1). After the early-nucleated dislocations escaped from the sample surface, more dislocation sources nucleated from different sites on the surface and the predeposited dislocations. During the plastic flow, interactions between dislocations can slow down the motion of dislocations and facilitate the dislocation accumulation within the layered phase as shown in Figure (b-iv). In addition, dislocations are relatively uniform distributed within each layer, which implies the multiple slips have been activated in the 5.0 nm sample.

While for $h < h_c$, the dislocation structure is highly localized along a single slip trace propagating through the whole sample. From Fig. 2 (b-I')-(b-iv'), we can see the shear localization started from the early-nucleated dislocations and then become longer and

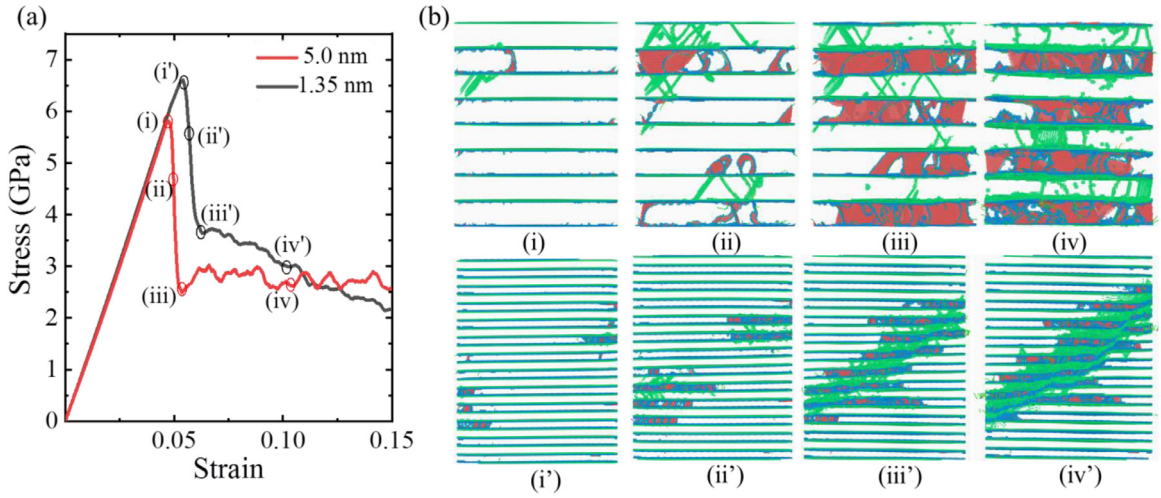

Fig. 2. (a) Stress–strain curves for samples with h = 1.35 nm and 5.0 nm at T = 10k. (b) The configuration of the dislocation structures at different strains (i)–(iv) and (i')–(iv') marked by circles in (a). (Cu atoms are in blue, Nb atoms are in green, atoms (HCP) on stacking faults are in red. Perfect FCC, BCC atoms and the free surface atoms are not shown.)

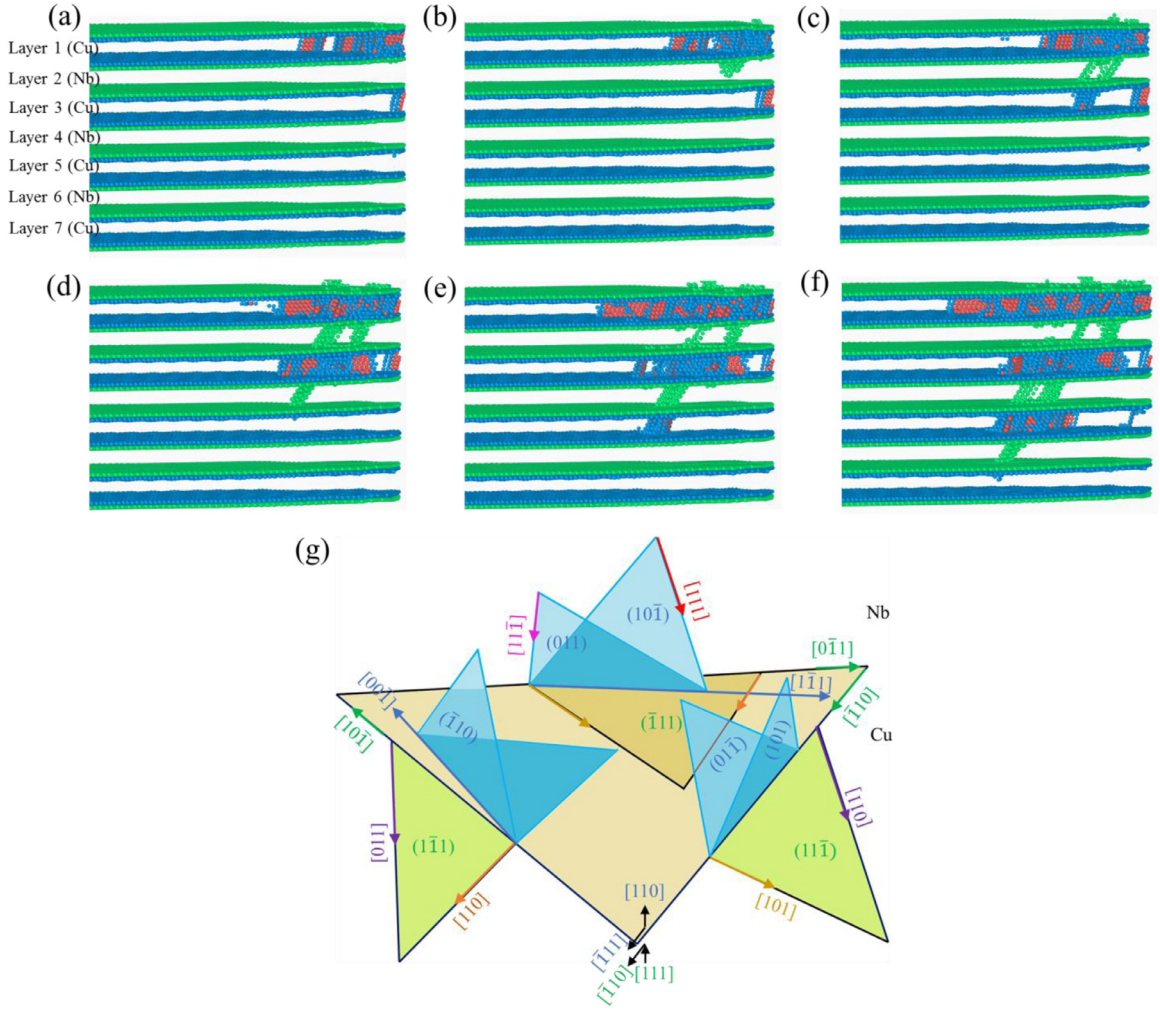

Fig. 3. Side views of atomistic configurations for dislocation slip transmission events in the sample with h = 1.35 nm. Images (a–f) correspond to applied strains at 5.20%, 5.27%, 5.30%, 5.34%, 5.36% and 5.39%, respectively. Atoms are colored by CAN. (g) Schematic plot of slip systems of Cu/Nb MNCs with KS orientation relationship (The interface plane is (111) FCC–Cu || (110) BCC–Nb. Three {111} glide planes in Cu and five {110} glide planes in Nb that are non-parallel to the interface plane).

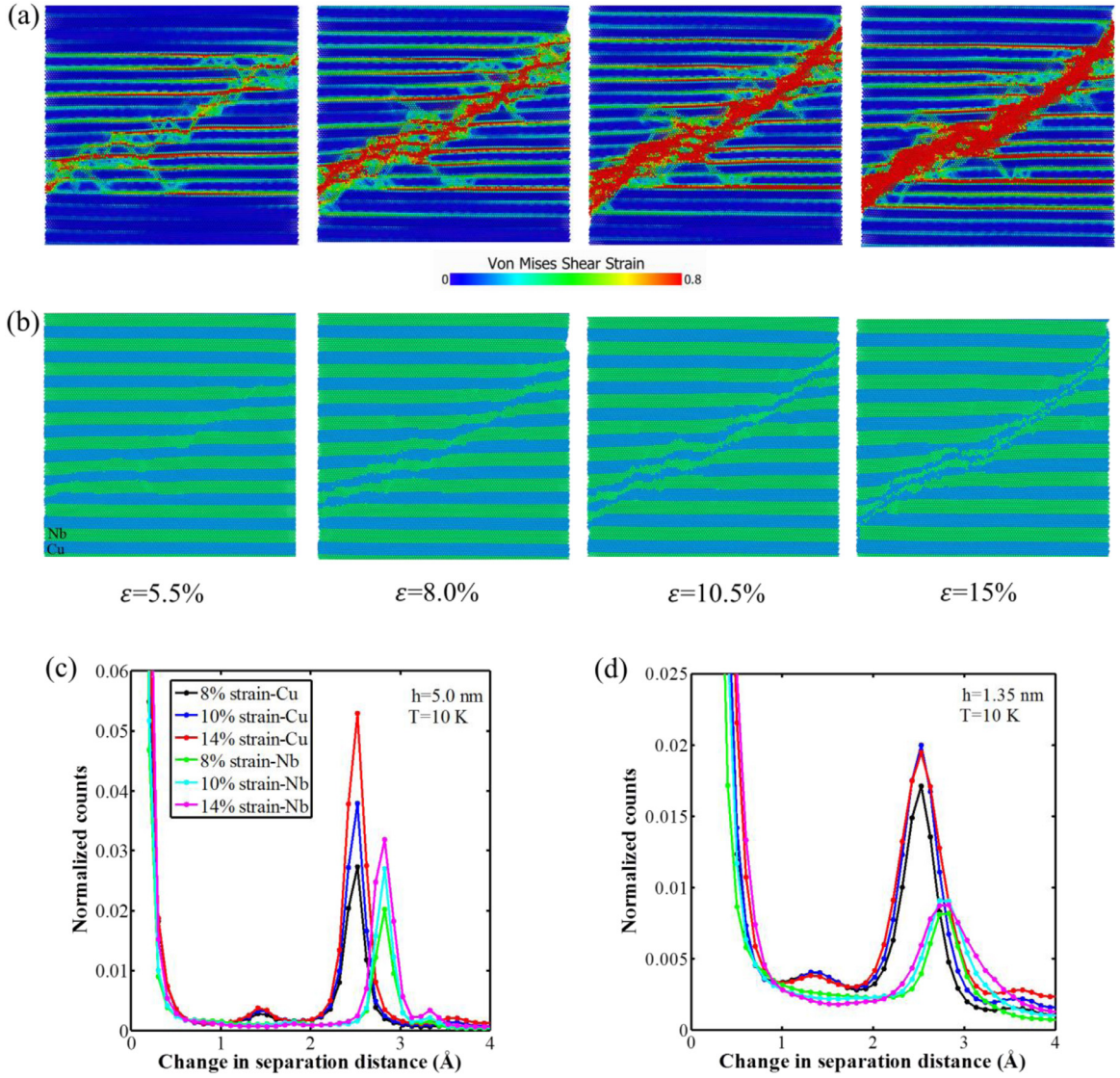

Fig. 4. Sequential snapshots of (a) von Mises shear strain distributions and (b) atomistic configurations for the 1.35 nm sample at different strain levels. Change in the separation distance of initially nearest neighbor atoms at different strains for (c) 5.0 nm and (d) 1.35 nm.

wider with increment of strain. In our simulations, shear localization only appeared in samples with the layer thickness below h_c ($\approx$ 2.0 nm). This trend is consistent with recent pillar compression results, in which pillars with $h >$ 2.0 nm does not show any shear bands on the deformed samples, nor does the stress-strain data show any load drops during the test [43].

To understand the formation of the localized dislocation structure, we examined the atomistic configurations for dislocation transmission events in the 1.35 nm sample shown in Fig. 3. The nucleation of dislocation started in the layer 1 (Cu) on the intersection between the free surface and interface same as those observed in the 5.0 nm sample. However, those early nucleated dislocations were pinned by the two adjacent interfaces, as the critical stress driving dislocation move in such a thin layer thickness is high. With the increment of the load, new dislocations nucleated from the interface nearby the early-nucleated ones. Then one of those immobile dislocations in the Cu phase transmitted across the interface and activated one dislocation in the layer 2 (Nb). Although the newly activated dislocation in Nb phase cannot glide through the whole phase, its expansion from one interface to the opposite one still generated plastic strain in the Nb phase. When the dislocation in Nb phase approached the bottom interface in layer 2 (Nb), it promoted the nucleation of a dislocation within layer 3 (Cu). This dislocation nucleation and transmission process repeatedly occurred from one layer to another and resulted in the highly localized dislocation structure.

After analyzing the slip systems of the dislocation across the interface, we found the transmission always occurs on the $(11\bar{1})$ slip plane in FCC Cu and $(01\bar{1})$ slip plane in BCC Nb. From Fig. 3(g), we can see, for the KS orientation relationship, only $(11\bar{1})$ slip plane in Cu and $(01\bar{1})$ slip plane in Nb carry the parallel trace ($[\bar{1}11]$ || $[\bar{1}10]$) on the interface plane. When incoming dislocations approach the interface, it is relatively easier for those on the slip plane with the parallel slip trace transmit from one phase to another phase, as the energy barrier is lower for the transmission between those two slip planes [45]. Since the dislocation transmission only occurred on one plane in both Cu and Nb phases, the crystal lattice gradually rotated off its original orientation that induced further activities on the interface, such as the interface sliding, and promoted the shear band formation.

Fig. 4(a) shows the local von Mises shear strain in the sample with h = 1.35 nm at different strain levels. The Von Mises shear

strain was calculated based on the method developed in [46]. It is obvious that the initial shear localization started from the dislocation nucleation and transmission. Then, the shear band was developed following the early shear localization and intensified and thickened with the increment of the applied strain. While no significant plasticity occurred away from the shear band. This shear band formation mechanism is similar to that found in NC metals, in which the shear band developed along early localization nearby GBs [47]. However, there is no or few GBs in MNCs, the major plastic deformation can only be accommodated by either dislocation gliding or the interface sliding or both of them [48]. In addition, the shear band observed in study is also different from an amorphous shear band developed in Cu/Zr metallic glass system [49], as the Cu and Nb phases are still well separated within the shear band as shown in Fig. 4(b).

To identify the activities within the shear band, the change in the separation distance of initially nearest neighbor atoms is analyzed and shown in Fig. 4(c) and (d). All peak values in Fig. 4(c) and (d) indicate dominant relative displacements of atoms in the crystal during deformation. In both plots, the two highest peaks respectively appear at about 0.25 Å and 0.28 Å, which corresponds to the Burgers vectors of full lattice dislocations for Cu and Nb crystals.

From Fig. 4(c), we can see, in the 5.0 nm sample, the height of peaks increases with the strain in both phases. That indicates that the dislocation provided the major contribution to the plastic deformation in the samples. And the dislocation activities were intensified with the increment of strain. While, in Fig. 4(d), the heights of peaks for $h = 1.35$ nm are much lower than those for $h = 5.0$ nm. For example, the heights of peaks at 0.25 Å and 0.28 Å are about 0.017 and 0.008 at 8% strain for $h = 1.35$ nm, in contrast to those about 0.0285 and 0.021 for $h = 5.0$ nm at the same strain. That means the plastic strain induced by the dislocation is less in thinner layers. In addition, the difference between the peak heights for the two different layer thicknesses was enlarged at higher strains. In Fig. 4(d), the peaks for 10% and 14% almost overlap each other in both Cu and Nb phases. That implies there was almost no plastic strain contributed from dislocation gliding in the sample with $h = 1.35$ deformed beyond 10% strain. Since the shear band has already formed at 10% strain as shown in Fig. 4(a)-(b), it is not hard to conclude that the interface sliding rather than dislocation gliding dominates the plastic flow within the shear band and that intensified the shear band in samples with $h < h_c$. It is worthy to mention that the layer thickness, crystal structure of each layer and orientation relationship between each phase are three key factors affecting the mechanical behavior of MNCs [50–52]. For instance, the Cu/Au (FCC/FCC) possesses different crystal structure and orientation relationship from the Cu/Nb (FCC/BCC) system. And the value of h_c in Cu/Nb revealed in this study is much lower than that in Cu/Au system [53,54]. Further systematic studies are needed to establish the quantitative relationships between the shear localization in MNCs and their layer thickness, crystal structure and orientation relationships.

In summary, we explored the effect of the layer thickness on the shear localization and shear band formation in Cu/Nb MNCs via MD simulations. The simulation results show that Cu/Nb MNCs exhibit increasing strength with decreasing layer thickness to a critical thickness equal to 2.0 nm, blow which the strength decreases with the layer thickness. The inverse size effect below the critical thickness is induced by the shear localization. The quantitative analysis revealed that the unsymmetrical dislocation transmission across the interface induces the shear localization and promotes the shear band formation in Cu/Nb MNCs with layer thickness below h_c. Within the shear band, the plastic strain mainly comes from the interface sliding rather than dislocation gliding. Our work revealed the origin of the shear band formation in Cu/Nb MNCs and can shed light on the design of MNCs with superior mechanical properties.

Declaration of Competing Interest

The authors declare that they have no known competing financial interests or personal relationships that could have appeared to influence the work reported in this paper.

Acknowledgements

This work was supported by the grants from NSF CAREER Award (CMMI-1652662). This work was performed, in part, at the Center for Integrated Nanotechnologies, an Office of Science User Facility operated for the U.S. Department of Energy (DOE) Office of Science. Los Alamos National Laboratory, an affirmative action equal opportunity employer, is managed by Triad National Security, LLC for the U.S. Department of Energy's NNSA, under contract 89233218CNA000001. The supercomputer time allocation was provided by XSEDE (DMR170093).

Supplementary materials

Supplementary material associated with this article can be found, in the online version, at doi:10.1016/j.scriptamat.2020.06.049.

References

[1] by J.E. Mahan, in: John E. Mahan (Ed.), Physical Vapor Deposition of Thin Films, Wiley-VCH, 2000, p. 336. byISBN 0-471-33001-9January 2000336.
[2] G.S. Was, T. Foecke, Thin Solid Films 286 (1996) 1–31.
[3] C.A. Ross, Annu. Rev. Mater. Sci. 24 (1994) 159–188.
[4] N. Tsuji, Y. Saito, S.H. Lee, Y. Minamino, Adv. Eng. Mater. 5 (2003) 338–344.
[5] J.S. Carpenter, S.C. Vogel, J.E. Ledonne, D.L. Hammon, I.J. Beyerlein, N.A. Mara, Acta Mater. 60 (2012) 1576–1586.
[6] S. Zheng, I.J. Beyerlein, J.S. Carpenter, K. Kang, J. Wang, W. Han, N.A. Mara, Nat. Commun. 4 (2013).
[7] M.J. Demkowicz, R.G. Hoagland, J.P. Hirth, Phys. Rev. Lett. 100 (2008).
[8] J. Wang, R.G. Hoagland, J.P. Hirth, A. Misra, Acta Mater. 56 (2008) 5685–5693.
[9] J.Y. Zhang, X. Zhang, R.H. Wang, S.Y. Lei, P. Zhang, J.J. Niu, G. Liu, G.J. Zhang, J. Sun, Acta Mater. 59 (2011) 7368–7379.
[10] A. Misra, M.J. Demkowicz, X. Zhang, R.G. Hoagland, JOM 59 (2007) 62–65.
[11] A. Misra, J.P. Hirth, R.G. Hoagland, Acta Mater. 53 (2005) 4817–4824.
[12] A. Misra, M.J. Demkowicz, J. Wang, R.G. Hoagland, JOM 60 (2008) 39–42.
[13] P.M. Anderson, C. Li, Nanostruct. Mater. 5 (1995) 349–362.
[14] A. Misra, M. Verdier, Y.C. Lu, H. Kung, T.E. Mitchell, M. Nastasi, J.D. Embury, Scr. Mater. 39 (1998) 555–560.
[15] Y. Cui, B. Derby, N. Li, N.A. Mara, A. Misra, Mater. Res. Lett. 6 (2018) 184–190.
[16] F. Wang, P. Huang, M. Xu, T. Lu, K. Xu, Mater. Sci. Eng. 528 (2011) 7290–7294.
[17] X. Zhu, J. Luo, F. Zeng, F. Pan, Thin Solid Films 520 (2011) 818–823.
[18] T. Wynn, D. Bhattacharyya, D. Hammon, A. Misra, N. Mara, Mater. Sci. Eng. 564 (2013) 213–217.
[19] N.A. Mara, D. Bhattacharyya, J.P. Hirth, P. Dickerson, A. Misra, Appl. Phys. Lett. 97 (2010).
[20] S.M. Han, M.A. Phillips, W.D. Nix, Acta Mater. 57 (2009) 4473–4490.
[21] D. Bhattacharyya, N. Mara, P. Dickerson, R. Hoagland, A. Misra, J. Mater. Res. 24 (2009) 1291–1302.
[22] Y. Kim, A.S. Budiman, J.K. Baldwin, N.A. Mara, A. Misra, S.M. Han, J. Mater. Res. 27 (2012) 592–598.
[23] J. Wang, R. Hoagland, X. Liu, A. Misra, Acta Mater. 59 (2011) 3164–3173.
[24] Y. Li, X. Zhu, G. Zhang, J. Tan, W. Wang, B. Wu, Philos. Mag. 90 (2010) 3049–3067.
[25] P. Dayal, M.Z. Quadir, C. Kong, N. Savvides, M. Hoffman, Thin Solid Films 519 (2011) 3213–3220.
[26] S. Zheng, J. Wang, J. Carpenter, W. Mook, P. Dickerson, N. Mara, I. Beyerlein, Acta Mater. 79 (2014) 282–291.
[27] X. Chen, X. Kong, A. Misra, D. Legut, B. Yao, T. Germann, R. Zhang, Acta Mater. 143 (2018) 107–120.
[28] J. Wang, R. Zhang, C. Zhou, I.J. Beyerlein, A. Misra, J. Mater. Res. 28 (2013) 1646–1657.
[29] S. Shao, J. Wang, A. Misra, R.G. Hoagland, Sci. Rep. 3 (2013) 2448.
[30] K. Kang, J. Wang, I. Beyerlein, J. Appl. Phys. 111 (2012) 053531.
[31] R. Zhang, I. Beyerlein, S. Zheng, S. Zhang, A. Stukowski, T. Germann, Acta Mater. 113 (2016) 194–205.
[32] J. Wang, R. Zhang, C. Zhou, I.J. Beyerlein, A. Misra, Int. J. Plast. 53 (2014) 40–55.
[33] J. Wang, A. Misra, R. Hoagland, J. Hirth, Acta Mater. 60 (2012) 1503–1513.
[34] J. Wang, R. Hoagland, J. Hirth, A. Misra, Acta Mater. 56 (2008) 5685–5693.

[35] J. Wang, R. Hoagland, J. Hirth, A. Misra, Acta Mater. 56 (2008) 3109–3119.
[36] K. Kang, J. Wang, S. Zheng, I. Beyerlein, J. Appl. Phys. 112 (2012) 073501.
[37] A. Misra, J. Hirth, R. Hoagland, J. Embury, H. Kung, Acta Mater. 52 (2004) 2387–2394.
[38] L. Zhang, E. Martinez, A. Caro, X.-Y. Liu, M.J. Demkowicz, Model. Simul. Mater. Sci. Eng. 21 (2013) 025005.
[39] J.D. Honeycutt, H.C. Andersen, J. Phys. Chem. 91 (1987) 4950–4963.
[40] M.S. Daw, M.I. Baskes, Phys. Rev. B 29 (1984) 6443.
[41] A. Stukowski, Model. Simul. Mater. Sci. Eng. 18 (2009) 015012.
[42] C. Brandl, P.M. Derlet, H. Van Swygenhoven, Philos. Mag. 89 (2009) 3465–3475.
[43] N. Li, N. Mara, Y. Wang, M. Nastasi, A. Misra, Scr. Mater. 64 (2011) 974–977.
[44] N. Li, N.A. Mara, J. Wang, P. Dickerson, J. Huang, A. Misra, Scr. Mater. 67 (2012) 479–482.
[45] I.J. Beyerlein, J. Wang, R. Zhang, Acta Mater. 61 (2013) 7488–7499.
[46] M.L. Falk, J.S. Langer, Phys. Rev. E 57 (1998) 7192–7205.
[47] T.J. Rupert, J. Appl. Phys. 114 (2013) 033527.
[48] S. Shao, C. Zhou, A. Misra, J. Wang, Handbook of Materials Modeling: Methods: Theory and Modeling, 2018, pp. 1–30.
[49] D.D. Alix-Williams, M.L. Falk, Phys. Rev. E 98 (2018) 053002.
[50] S. Shao, C. Zhou, A. Misra, J. Wang, Handbook of Materials Modeling: Methods: Theory and Modeling, 2020, pp. 1049–1078.
[51] J. Wang, A. Misra, Curr. Opin. Solid State Mater. Sci. 15 (2011) 20–28.
[52] M.J. Buehler, A. Misra, MRS Bull. 44 (2019) 19–24.
[53] Y. Li, X. Zhu, J. Tan, B. Wu, W. Wang, G. Zhang, J. Mater. Res. 24 (2009) 728–735.
[54] A. Gola, G.-P. Zhang, L. Pastewka, R. Schwaiger, MRS Commun. 9 (2019) 1067–1071.